PAPER • OPEN ACCESS

Characterization of non-relativistic attosecond electron pulses by transition radiation from tilted surfaces

To cite this article: M V Tsarev and P Baum 2018 *New J. Phys.* **20** 033002

New Journal of Physics
The open access journal at the forefront of physics

Deutsche Physikalische Gesellschaft DPG
IOP Institute of Physics

Published in partnership with: Deutsche Physikalische Gesellschaft and the Institute of Physics

OPEN ACCESS

RECEIVED
11 August 2017

REVISED
15 January 2018

ACCEPTED FOR PUBLICATION
7 February 2018

PUBLISHED
5 March 2018

PAPER

Characterization of non-relativistic attosecond electron pulses by transition radiation from tilted surfaces

M V Tsarev and P Baum

Max-Planck-Institute of Quantum Optics, Hans-Kopfermann-Str. 1, D-85748 Garching, Germany

E-mail: peter.baum@lmu.de

Keywords: ultrafast electron diffraction, attosecond science, transition radiation

Abstract

We consider analytically and numerically the emission of coherent transition radiation by few-femtosecond and attosecond electron pulses. With optimized geometries based on tilted surfaces we avoid the influences of the beam diameter and velocity mismatch for sub-relativistic pulses. We predict the emission of visible and ultraviolet optical radiation that characterizes few-femtosecond or attosecond electron pulses in time. The total amount of radiation depends on the source' repetition rate and number of electrons per macro/microbunch and is in many cases sufficient for pulse length characterization in the emerging experiments.

1. Introduction

Ultrashort electron pulses with picosecond, femtosecond or attosecond duration are central to a wide variety of scientific and technological applications. For example, they allow via pump-probe electron microscopy [1–4] and diffraction [5–10] the tracking of atomic and electronic motion in space and time, they produce coherent x-ray pulses in free-electron lasers [11], they are central to laser-driven particle acceleration [12] or they serve as probes of quantum dynamics of the electron [13]. Reaching peak performance in these studies often requires shortest possible pulse durations [14]. Femtosecond electron pulses can be produced by laser-driven photocathodes [15–17] or needle tips [18, 19]. Few-femtosecond duration is achievable by radio-frequency compression [20–23] or all-optical terahertz techniques [24]. At relativistic energies, few-femtosecond and attosecond durations have been achieved by inverse free-electron laser processes [25] and laser-wakefield accelerators [26–29]. Sub-relativistic electron pulses of attosecond durations can be made by ponderomotive forces in standing laser waves [30, 31] or by time-varying electric fields [32–34]; see figure 1 for an overview. Such sub-relativistic attosecond electron pulses, which have a de Broglie wavelength that is well suited for atomic-scale imaging [14], will advance ultrafast diffraction and microscopy to the time range of atomic-scale electron dynamics [35–38] and may also push forward other applications, including quantum state reconstruction [33], into novel resolution regimes. Recently, attosecond electron diffraction and microscopy could indeed be demonstrated in an experiment [34].

A prerequisite for applying few-femtosecond or attosecond electron pulses to studies of light–matter interaction is a proper characterization of temporal shape and duration. A widespread method in electron-pulse metrology is a spectrally resolved measurement of coherent transition radiation (CTR) [39–49], i.e. recording and analyzing the electromagnetic fields that are emitted by a multi-electron bunch that hits an interface between media of different refractive index [40, 50]. In principle, shorter electron pulses produce higher frequencies and the shortest optical wavelength that is recorded indicates the pulse duration. However, in practical experiments, the emitted spectrum is often substantially restricted in the short-wavelength region by the influence of the lateral size of the electron beam at the interface [51], which causes destructive optical interference. This high-frequency cutoff restricts the applicability of CTR pulse-length characterizations to electron beams with very small lateral dimensions [48] or beams at highly relativistic energies [25–29]. Unfortunately, the ultrashort electron pulses in ultrafast atomic-scale diffraction need sub-relativistic energies

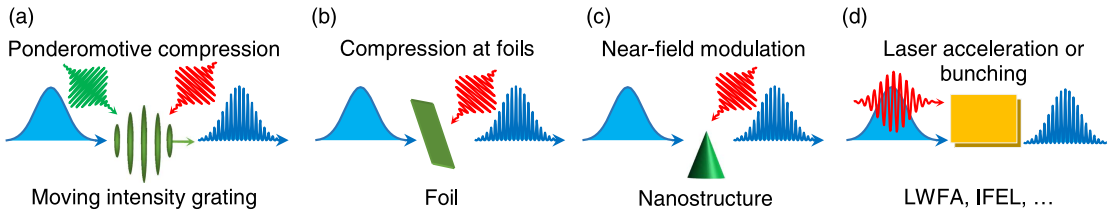

Figure 1. Some concepts for generating attosecond electron pulses. (a) A two-color light field generates a traveling intensity grating that causes ponderomotive compression to attosecond duration [30, 31, 57]. (b) A laser pulse that is incident on a metal foil is reflected and electrons experience a cycle-dependent acceleration or deceleration by the laser's electric fields [24, 56], producing attosecond pulses [32–34]. (c) Similarly, a well-focused electron beam passing close to a laser-excited nanostructure can also experience time-dependent forces and temporal compression [58]. (d) Inverse free-electron laser process or laser-wakefield accelerators can also produce few-femtosecond or attosecond electron pulses [25–29].

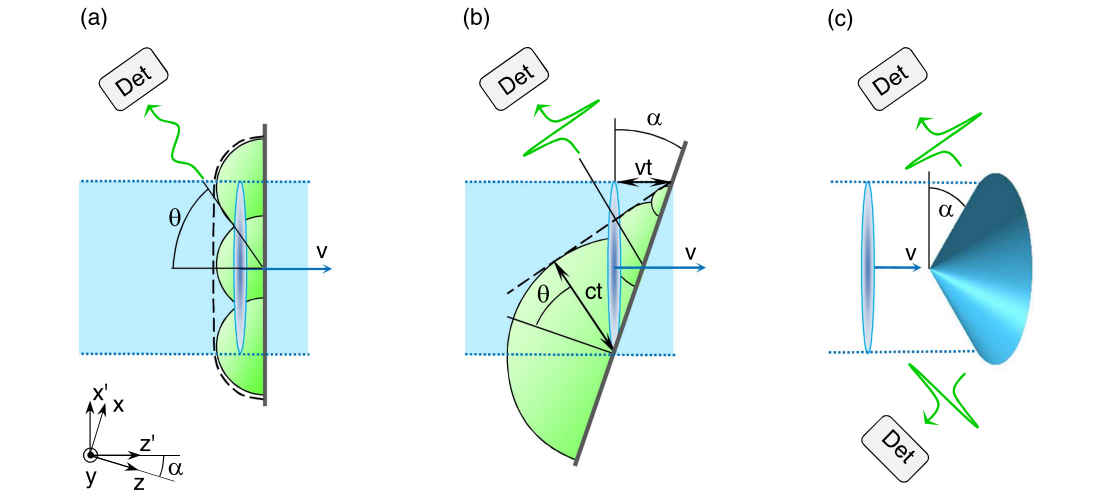

Figure 2. Concept of using coherent transition radiation (CTR) for detection of ultrashort electron bunches. (a) For normal incidence, the maximal frequency of emission is determined by the lateral size of an ultrashort bunch and not by its duration. Inset, coordinate system. (b) For a properly tilted surface, velocity matching provides in-plane constructive interference for all frequencies emitted to a certain angle independently of the lateral size of the bunch (x'). (c) A conically-shaped surface in a cylindrical geometry completely eliminates the beam's transverse-size influences (x' and y) on the CTR spectrum.

(tens to hundreds of keV) in order to provide a suitable de Broglie wavelength for atomic diffraction [52]. The beam diameter is typically at least tens-of-μm [52–54]. Characterization of few-femtosecond electron pulses has therefore only been possible with laser-based methods, for example by a terahertz oscilloscope [24], via ponderomotive scattering [55] or laser streaking [21, 56].

In this report we analytically and numerically investigate to what extent CTR may be useful for characterizing non-relativistic electron pulses of few-femtosecond and eventually attosecond duration. First we report a tilted-surface or conical emission geometry that solves velocity-matching problems and avoids any high-frequency cutoff. Second, we predict for realistic materials (Ag or Si) the emission of visible and even ultraviolet transition radiation that directly reveals few-femtosecond or attosecond pulse durations. Third, we numerically estimate the overall useful photon flux that can be expected for several realistic electron sources and estimate the required averaging time in an experiment. We conclude with an outlook on the value of transition radiation in case that few-attosecond or even shorter electron pulses would eventually be generated, where characterization with lasers seems unrealistic.

2. Methods

Figure 2 illustrates the basic problem and our solution. Suppose that an electron beam (blue) hits a foil or surface (black) at normal incidence (see figure 2(a)). A short pulse of finite beam diameter impinges everywhere at the same time and each part (each single electron) emits coherently with a single-cycle behavior in time and therefore with a broadband spectrum. However, at an off-axis detector (gray box), which is required because transition ration is not emitted in backwards direction [59], the individual single-electron emissions interfere in part destructively as a consequence of the finite beam diameter. In a simplified picture, the highest frequency

that the detector can see depends on the projected bunch size into detection direction. Therefore a convolution of the time-domain pulse duration with the lateral-domain beam size is measured, and not the pulse duration alone as intended.

In contrast, if the surface is tilted by a properly chosen angle α (see figure 2(b)), the incident ultrashort pulse (blue ellipse) impinges with an effective velocity along the surface. Therefore all individual dipole emissions (single-cycle in time and broadband) obtain a linear delay and can arrive coherently at a given detector angle with constructive interference and in temporal synchrony (see dashed line in figure 2(b)). The highest detected frequency is now independent of the beam diameter and solely depends on the electron pulse duration in propagation direction. Visible and ultraviolet radiation can therefore be expected for attosecond electron pulses.

The proper tilt angle α depends on the electron velocity and can be derived via the Huygens principle by the construction in figure 2(b). Constructive interference occurs at a detector angle θ if

$$v \sin\theta = c \sin\alpha, \tag{1}$$

where v is the electron velocity and c is the speed of light. This velocity matching condition is frequency-independent. The remaining influence of a finite beam size is that it creates a collimated beam of high-frequency emission and therefore restricts the angular acceptance, i.e. the detector size, for which the above mentioned constructive interference occurs.

Figure 2(c) shows another variant of such a structure, namely a conical surface with an angle α. Given a collimated electron beam, the cylindrical symmetry assures velocity-matched CTR emission over the entire two-dimensional profile of an extended electron beam. Collection of the resulting conical emission pattern (green) with a ring-shaped detector is a very efficient way of obtaining pulse duration information without losses (see below).

We continue to formulate an analytical set of equations to support our tilted-surface ideas. It was shown [50, 51] that for a bunch of N electrons the energy of transition radiation that is emitted per unit solid angle and per unit frequency interval is given by

$$W_{\Omega,\omega}(k_x, k_y, k_z) = W^1_{\Omega,\omega}(k_x, k_y, k_z) \times [N + N(N-1)\,|\tilde{f}(k_x, k_y, k_z)|^2], \tag{2}$$

where $W^1_{\Omega,\omega}(k_x, k_y, k_z)$ is the emission spectrum of a single particle (see appendix A) and where $\tilde{f}(k_x, k_y, k_z)$ is the normalized-to-unity Fourier-transform of the charge density in the bunch. The wavenumbers k_x, k_y, and k_z (see the coordinates in figures 2(a) and (b)) define the angle of observation and the frequency of emission. In equation (2), the first term in the brackets constitutes the incoherent part of radiation while the second term is the CTR. For a sufficiently large number of electrons in a single bunch, the incoherent part can be neglected and equation (2) becomes [59]

$$W_{\Omega,\omega} \approx W^1_{\Omega,\omega}\, N^2\, |\tilde{f}|^2. \tag{3}$$

This equation has some useful analogy with dipole antenna arrays, where $W^1_{\Omega,\omega}$ corresponds to the emission pattern of a single antenna and where $|\tilde{f}|^2$ is the array factor. In the CTR case, the factor $W^1_{\Omega,\omega}$ is fully determined by the complex refractive index of the surface material (see appendix A for details) and the velocity v of the bunch, while $|\tilde{f}|^2$ depends on the spatial and temporal distribution of charge in the bunch. Both factors affect the directivity and the spectrum of the emitted radiation. The pulse-shape factor $|\tilde{f}|^2$ is always less than unity and can serve as a measure of suppression of high-frequency components in the CTR spectrum in comparison with the single-particle spectrum. To find the full radiated energy per pulse, one can use

$$W = \int_0^\infty \mathrm{d}\omega \int W_{\Omega,\omega}\mathrm{d}\Omega, \tag{4}$$

where $\mathrm{d}\Omega = \sin\theta\ \mathrm{d}\theta\mathrm{d}\varphi$ is the solid angle interval and where θ and φ are the polar and the azimuthal (out-of-incidence-plane) angles with respect to coordinates (x, y, z) (see figure 2(a), inset), respectively. We will in the following also use integrated quantities for the frequency spectrum $W_\omega = \int_{-\pi/2}^{\pi/2} W_{\Omega,\omega}|_{\varphi=0} \sin\theta\ \mathrm{d}\theta$ in the plane of incidence, as well as the polar $W_\theta = \int_0^\infty W_{\Omega,\omega}|_{\varphi=0}\mathrm{d}\omega$ and the azimuthal $W_\varphi = \int_0^\infty W_{\Omega,\omega}|_{\theta=\mathrm{const}}\mathrm{d}\omega$ angular distributions.

To analyze the properties of radiation in the case of the tilted interface (figure 2(b)), we have to find the form-factor $|\tilde{f}|^2$ in equation (3) for this case. We assume a uniformly moving non-dispersing bunch (for applicability of this approximation, see Discussion). Charge density depends on $\xi = z' - vt$ and is given by

$$\rho(x', y, z', t) = \rho(x', y, \xi). \tag{5}$$

We find the Fourier transform $\tilde{\rho}$ of the charge density (5) with respect to the coordinates (x, y, z),

$$\tilde{\rho}(k_x, k_y, k_z) = \frac{1}{(2\pi)^3}\int_{-\infty}^{\infty} \rho(x', y, \xi)\mathrm{e}^{-\mathrm{i}k_x x - \mathrm{i}k_y y - \mathrm{i}k_z z}\mathrm{d}x\mathrm{d}y\mathrm{d}z \tag{6}$$

and conveniently re-write it via the Fourier transform $\tilde{\rho}'$ in the bunch's coordinate system (x', y, ξ):

$$\tilde{\rho}(k_x, k_y, k_z) = \mathrm{e}^{-\mathrm{i}vt(k_x \sin\alpha + k_z\cos\alpha)} \times \tilde{\rho}'(k_x\cos\alpha - k_z\sin\alpha, k_y, k_x\sin\alpha + k_z\cos\alpha). \tag{7}$$

Eliminating k_z from (7) by using the condition $k_x v_x + k_z v_z = \omega$ that holds for radiated fields and defines the emitted frequency ω [60], we arrive at a formula that connects the Fourier-transforms in the surface's and in the bunch's coordinates,

$$\tilde{\rho}(k_x, k_y, k_z) = \mathrm{e}^{-\mathrm{i}\omega t}\,\tilde{\rho}'\left(\Delta k, k_y, \frac{\omega}{v}\right). \tag{8}$$

Using equation (8), one can readily obtain Fourier distribution $\tilde{\rho}$ required by equation (3) in the surface coordinates (x, y, z) by taking a Fourier transform $\tilde{\rho}'$ of the bunch's density in coordinates (x', y, ξ) and substituting proper wavenumbers. In equation (8)

$$\Delta k = \left(k_x - \frac{\omega}{v}\sin\alpha\right)\Big/\cos\alpha \tag{9}$$

is the new effective transverse wavenumber and ω/v is the respective longitudinal wavenumber. The emitted CTR spectrum given by equation (3) is $W_{\Omega,\omega} \sim |\tilde{f}|^2 \sim |\tilde{\rho}|^2$, while, at the velocity matching condition, $\Delta k = 0$, $\tilde{\rho} \sim \int \rho(x')\exp(-\mathrm{i}\,\Delta k x')\mathrm{d}x' = \int(\rho(x')\mathrm{d}x')$ according to equation (8). This means that at the correct velocity matching angle the CTR spectrum $W_{\Omega,\omega}$ depends only on the overall charge of the bunch, but not any more on its lateral size (along x') or any particular distribution. Using $k_x = \frac{\omega}{c}\sin\theta\cos\varphi$, the condition of velocity matching $\Delta k = 0$ can be rewritten as equation (1) in the plane of incidence ($\varphi = 0$).

For our calculations of specific experimental cases that are reported below, we use Gaussian distributions of charge

$$\rho(x', y, \xi) = q/(\pi^{3/2} l_x l_y l_\parallel)\exp\left[-\left(\frac{x'}{l_x}\right)^2 - \left(\frac{y}{l_y}\right)^2 - \left(\frac{\xi}{l_\parallel}\right)^2\right]. \tag{10}$$

In the spectral domain, we obtain from equations (8) and (10) $\tilde{\rho}(k_x, k_y, k_z) = \frac{q}{(2\pi)^3}\tilde{f}$ with

$$\tilde{f}\left(\Delta k, k_y, \frac{\omega}{v}\right) = \mathrm{e}^{-\mathrm{i}\omega t}\mathrm{e}^{-\frac{1}{4}[l_x\Delta k]^2}\mathrm{e}^{-\frac{1}{4}l_y^2 k_y^2}\mathrm{e}^{-\frac{1}{4}l_\parallel^2\frac{\omega^2}{v^2}}. \tag{11}$$

Equation (11) is an explicit expression for the CTR suppression factor for an electron pulse with a Gaussian shape. It can be readily used for calculation of the CTR spectrum and energy via equations (2)–(4). Based on equation (11), a CTR spectral cutoff can also be defined (for example as $1/e^2$). From the Gaussian suppression factor given by equation (11), as well as from the discussion of equations (8) and (9) for an arbitrary-distributed pulse, or from figure 2(b) and equation (1), one can see that the condition $\Delta k = 0$ completely eliminates the influence of l_x on $\tilde{f}$, and therefore high-frequency components of $W_{\Omega,\omega}$ are not suppressed by the finite transverse size of the beam l_x. The spectrum at the velocity-matched angle ($\Delta k = 0$) and in the plane of incidence ($\varphi = 0$) depends only on the electron pulse duration and is maximized at

$$\lambda_{\mathrm{peak}} = \sqrt{2}\,\pi c\tau. \tag{12}$$

This equation directly relates the duration of an electron pulse with duration τ to the peak emission wavelength λ_{peak} which thus represents a measurable quantity that directly characterizes the pulse duration. For a non-Gaussian pulse shape, one can obtain the peak emission wavelength by calculating the Fourier transform $\tilde{f}(\omega)$ of the pulse shape $\rho(\xi)$ and maximizing $|\tilde{f}(\lambda)|^2/\lambda^2$.

The direct relation between λ_{peak} and τ of equation (12) holds, however, only for detection at velocity-matched angles. That means that for a small detector placed at such angle the high-frequency photon count per unit solid angle (and thus per pixel) will stay the same for any l_x and l_y, i.e. larger beams at the same local electron density will not emit more radiation. In order to estimate to what extent equation (12) is applicable to a spectrum integrated over the angles, we analyze the suppression factors in equation (11). The $1/e^2$ half-angle divergences of the CTR in the polar and azimuthal directions are evaluated from equation (11) and are, respectively, $\Delta\theta = \lambda/(\pi l_x\cos\theta/\cos\alpha)$ and $\Delta\varphi = \lambda/(\pi l_y)$. To avoid suppression of high frequencies in the integrated spectrum due to finite l_x and l_y, either the respective acceptance half-angles $\Delta\theta_{\mathrm{acc}}$ and $\Delta\varphi_{\mathrm{acc}}$ or the beam sizes must be small enough to satisfy the conditions $\Delta k l_x < 1$ and $k_y l_y < 1$, or, alternatively, $\Delta\theta_{\mathrm{acc}} < \Delta\theta/2$ and $\Delta\varphi_{\mathrm{acc}} < \Delta\varphi/2$. For example, assuming a 100 μm big detector located 10 cm away from the emission point, the above condition is satisfied for wavelengths down to $\lambda_{\mathrm{peak}} = 133$ nm (peak wavelength for 0.1 fs pulses

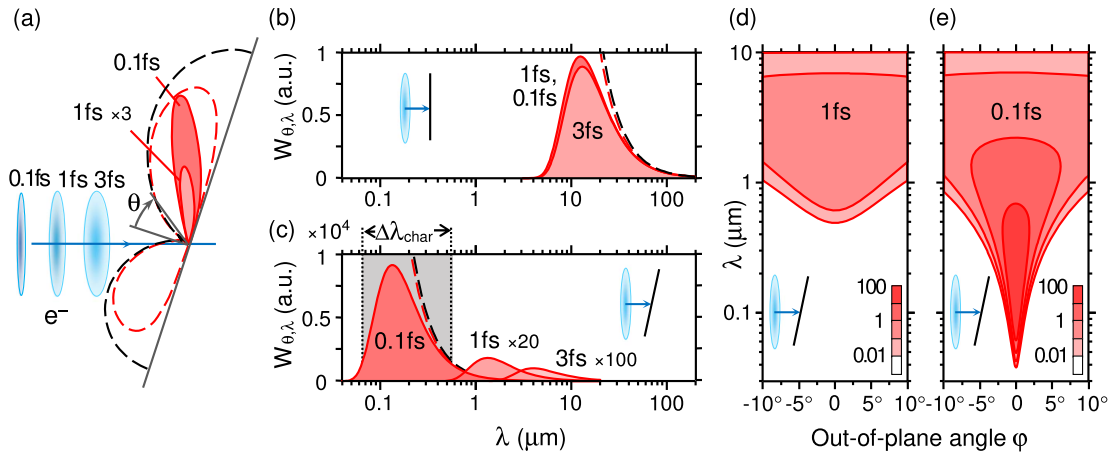

Figure 3. Frequency-angular spectra of CTR for three example pulse duration of 3, 1 and 0.1 fs (solid curves and shaded areas) and corresponding single-particle spectra $W^1_{\theta,\lambda}$ (dashed curves). Beam radius is $l_x = l_y = 3$ μm and results are compared for a near-ideal mirror (red curves) and ideal conductor (black dashed curves). (a) Radiation patterns $W_{\theta,\lambda}(\theta)$ (solid curves) at oblique incidence ($\alpha = 18°$) at $\lambda = 1$ μm and corresponding $W^1_{\theta,\lambda}$ (dashed curves) at $\varphi = 0$. (b) Spectra $W_{\theta,\lambda}(\lambda)$ at $\theta = 68°$ for a non-tilted surface ($\alpha = 0$). (c) Spectra $W_{\theta,\lambda}(\lambda)$ (solid curves) at $\theta = 68°$ for a properly tilted surface ($\alpha = 18°$) and corresponding $W^1_{\theta,\lambda}$ (dashed curves) at $\varphi = 0$. Note the scale differences; the peak emission in (c) is ~10^4 times stronger. Gray shaded region shows the characteristic wavelength range for the 0.1 fs pulses. (d) Characteristic out-of-plane emission $W_{\varphi,\lambda}$ at $\theta = 68°$ for the tilted surface and $\tau = 1$ fs pulse. (e) Characteristic out-of-plane emission for the same geometry but for an attosecond pulse ($\tau = 0.1$ fs).

at $v = 1/3\,c$) for beam sizes of $l_x = 110$ μm and $l_y = 40$ μm or smaller. For somewhat larger beams or acceptance angles, the detected spectra will be slightly red-shifted. Nevertheless, if l_x and l_y are known, the duration information can still be extracted for the CTR spectra using equation (11) or its counterpart for a non-Gaussian beam.

It is interesting that for large angles of emission θ the above conditions for l_x are satisfied easier than for l_y. As a result, for a decent mirror with large angles of emission (see the Results section), sizes of l_x as large as a few λ can be acceptable for obtaining a not-suppressed spectrum even at $\Delta\theta_{\rm acc} \sim 1$.

Is it possible to fully eliminate the spectral narrowing originating from finite l_y by invoking the cylindrical geometry of figure 2(c), i.e. letting the electron beam hit a cone-shaped interface with half-apex angle $\pi/2 - \alpha$. For this geometry and a Gaussian beam,

$$\tilde{f}\left(\kappa, \frac{\omega}{v}\right) = \mathrm{e}^{-\mathrm{i}\omega t}\mathrm{e}^{-\frac{1}{4}l_\perp^2(\Delta \mathrm{k})^2}\mathrm{e}^{-\frac{1}{4}l_\parallel^2\frac{\omega^2}{v^2}} \tag{13}$$

with $l_\perp$ the transverse size of the bunch, $\kappa = \frac{\omega}{c}\sin\theta$ the transverse wavenumber, and $\Delta k = \left(\kappa - \frac{\omega}{v}\sin\alpha\right)/\cos\alpha$. Equations (3) and (4) with $\tilde{f}$ given by equation (13) can be used to calculate the CTR emission. The total radiation yield as well as the yield in the important high-frequency region in the case of conical emission (figure 2(c)) will be larger than in the flat geometry of figure 2(b), because in the conical geometry any part of the beam in both lateral dimensions encounters a properly tilted surface for efficient high-frequency emission. On the other hand, collection of radially emitted transition radiation might be somewhat challenging in the experiment, but this geometry should be advantageous if the overall flux of electrons is rather limited, as probably expected for non-relativistic attosecond electron beams due to space-charge reasons [57].

3. Results

Figure 3 shows the radiation patterns and spectra for three different electron bunch durations $\tau = l_\parallel/v$ of 3, 1 and 0.1 fs as examples of ultrashort pulses that are realistic in experiments [21–24, 32–34]. We assume an electron velocity $v/c = \beta = 1/3$ that corresponds to electron energy $E \approx 31$ keV, a very convenient value for atomic-resolution diffraction. The calculation via equations (3) and (11) was performed for an interface between vacuum and a nearly ideal metal mirror ($\varepsilon' = 0$, $\varepsilon'' = -1000$) and for a beam with sizes $l_x = l_y = 3$ μm. Figure 3(a) shows the emitted radiation pattern (normalized to N^2) for p-polarized radiation at the wavelength $\lambda = 1$ μm in the plane of incidence (at $\varphi = 0$). S-polarization is absent at $\varphi = 0$. The efficiency of emission depends on the longitudinal size of the bunch $l_\parallel$ via the Gaussian factor in equation (11). For $l_\parallel\omega/v \ll 1$ (the lobe for $\tau = 0.1$ fs), the efficiency approaches the single-particle efficiency (dashed curve). The angular width of the lobe is determined by a Gaussian factor with $l_x\Delta k$ in equation (11). Figures 3(b) and (c) show the (normalized to unity) spectra of emission at an angle close to velocity-matching ($\theta = 68°$) in the case of non-tilted ($\alpha = 0$) and tilted ($\alpha = 18°$) interface, respectively. In these figures we use $W_{\theta,\lambda} = 2\pi c W_{\Omega,\omega}|_{\varphi=0}/\lambda^2$ and

the corresponding $W^1_{\theta,\lambda}$, and $W_{\varphi,\lambda} = 2\pi c W_{\Omega,\omega}|_\theta / \lambda^2$. In the non-tilted case (figure 3(b)), the spectrum is confined to long wavelengths. Indeed, in this case $l_\parallel \omega/v$ under the exponential in equation (11) can be neglected since it is much smaller than $l_x \Delta k = l_x k_x$. The spectrum is thus determined only by the transverse size of the bunch via $\exp[-(l_x k_x)^2]$ and has a cut-off at the wavelengths for which $l_x k_x \approx 1$ ($< \lambda \approx 2\pi l_x$). In the tilted-interface case (figure 3(c)), we have $l_x \Delta k \approx 0$ in equation (11) and thus the short-wavelength cutoff of the spectrum is directly determined by the electron pulse duration via $\lambda \approx 2\pi l_\parallel / \beta$ or $\omega \approx 1/\tau$ and not by any beam shape influences. For short, pancake-shaped, electron pulses ($l_\parallel \ll l_x$), the shortest emitted wavelength in the case of velocity matching is much smaller [$\sim \exp(l_x/l_\parallel)^2$] than in the case of improperly tilted surfaces. The very similar emission spectra of figure 3(b) show clearly that an experimental differentiation between 3, 1 and 0.1 fs pulses is almost impossible in a non-optimized setup (figure 2(a)), while it becomes obvious (see the spectra of figure 3(c)) with the properly tilted geometry (figures 2(b) and (c)). Gray shaded region in figure 3(c) shows the characteristic interval of emission $\Delta\lambda_{\text{char}}$ ($1/e^2$ level) calculated via equation (11).

Figures 3(d) and (e) show the spectrally resolved out-of-plane distributions of emission $W_{\varphi,\lambda}$ for $\tau = 1$ fs (figure 3(d)) and $\tau = 0.1$ fs (figure 3(e)) in case of a tilted surface (not with the conical scheme). We only consider here p-polarization, because the s-polarization maximum appears only at angles close to $\varphi \sim 90°$ and it is also ~30 times smaller. It can be seen from comparison of figure 3(d) (1 fs pulses) and figure 3(e) (0.1 fs pulses) that the spectral components that unambiguously characterize the attosecond pulses are expected to occur in a rather narrow out-of-plane-angles φ, as predicted above. Note that this narrowing of the characteristic emission direction can be entirely avoided by using the cone-shaped geometry (see figure 2(c)), because in this case the emission is obviously independent on the azimuthal angle φ; equation (13) is identical to equation (11) at $\varphi = 0$.

In summary, from the above calculations it is clear that attosecond electron pulses should emit visible and ultraviolet radiation if a properly tilted geometry is chosen, and that no substantial emission could be expected otherwise.

Figure 3(c) shows that the most characteristic wavelength region of CTR emission for 100 as pulses is 60–600 nm. In this region, it is not easy to make a perfect mirror, and it is therefore appropriate to numerically investigate what realistic materials will maximize the emitted high-frequency CTR that is characteristic of few-femtosecond and attosecond electron pulses. Crystalline silicon (Si) is available with atomically flat surfaces and has real and imaginary parts of the dielectric constant of Si$\langle 111 \rangle$ reaching values of ~40 in the relevant region [61, 62]. Alternatively we also consider silver (Ag), which is known from optical applications to be a decent mirror at visible wavelengths. Dielectric properties were taken from [63]. Aluminum might also be a good candidate for ultraviolet emission, but it is not studied here due to possible difficulties with its oxide layer.

We first consider Si and the emission of incoherent transition radiation. Figure 4(a) shows the angular-spectral distribution $W^1_{\theta,\omega} \equiv W^1_{\Omega,\omega}|_{\varphi=0}$ for $v/c = 1/3$ (31 keV) and $\alpha = 0°$ (non-tilted incidence). There is substantial emission in the wavelength range 100–500 nm, with a peak emission angle near $\theta \approx 63°$. This is the best angle for detector placement. Via equation (1), the velocity-matching angle at θ is $\alpha \approx 17°$. Figure 4(b) shows the coherent emission spectrum $W_{\theta,\omega} \equiv W_{\Omega,\omega}|_{\varphi=0}/N^2$ calculated by equation (3) for this best-tilted geometry. The bunch parameters are $l_x = 3$ μm and $\tau = 100$ as. One can see substantial coherent emission in the range of 200–500 nm. The peak wavelength of emission, ≈300 nm, is substantially greater than predicted by equation (12) for an ideal mirror (≈133 nm) because of the decrease in the Si dielectric constant at $\lambda < 200$ nm. Thus, to directly characterize pulses shorter than 0.2 fs with silicon, one needs to account for silicon's dielectric function. The $1/e^2$ angular width of emission in figure 4(b) is $\Delta\theta \approx 4°$.

In figures 4(c) and (d) we plot the same incoherent and coherent spectra as in figures 4(a) and (b), respectively, but for the case of a vacuum-Ag interface. Guided again by the maximum of incoherent emission around $\theta \approx 63°$, we find again $\alpha \approx 17°$ for the tilt angle. In the case of the Ag interface a strong coherent emission in the range of 500–1000 nm is observed. The $1/e^2$ angular width of emission in figure 4(d) is $\Delta\theta \approx 6.5°$.

The main advantage of silicon with respect to silver is evidently a higher emission in the ultraviolet range, where Ag has rather small absolute values of dielectric constant. CTR spectrum of the Ag interface is much less sensitive to the pulse duration for 0.1 fs bunches. However, we find that for bunches of ≈ 1 fs and above, a metallic interface such as Ag is beneficial due to higher dielectric constant in the visible and near-infrared range. The estimation for peak emission wavelength of equation (12) also works well for $\tau > 1$ fs and a metallic interface. In summary, available realistic materials are very well appropriate to characterize few-femtosecond or attosecond electron pulses via CTR measurements at tilted geometries.

The above considerations were made for $E \approx 31$ keV, a very convenient energy for atomic-scale diffraction and also suitable for ponderomotive electron compression in standing waves [30, 31]. However, higher energies might be preferable in transmission electron microscopy or in pump-probe diffraction, because thicker samples can be explored. In figure 5 we plot the optimal tilt angles α_{opt} that maximizes the emitted energy, the

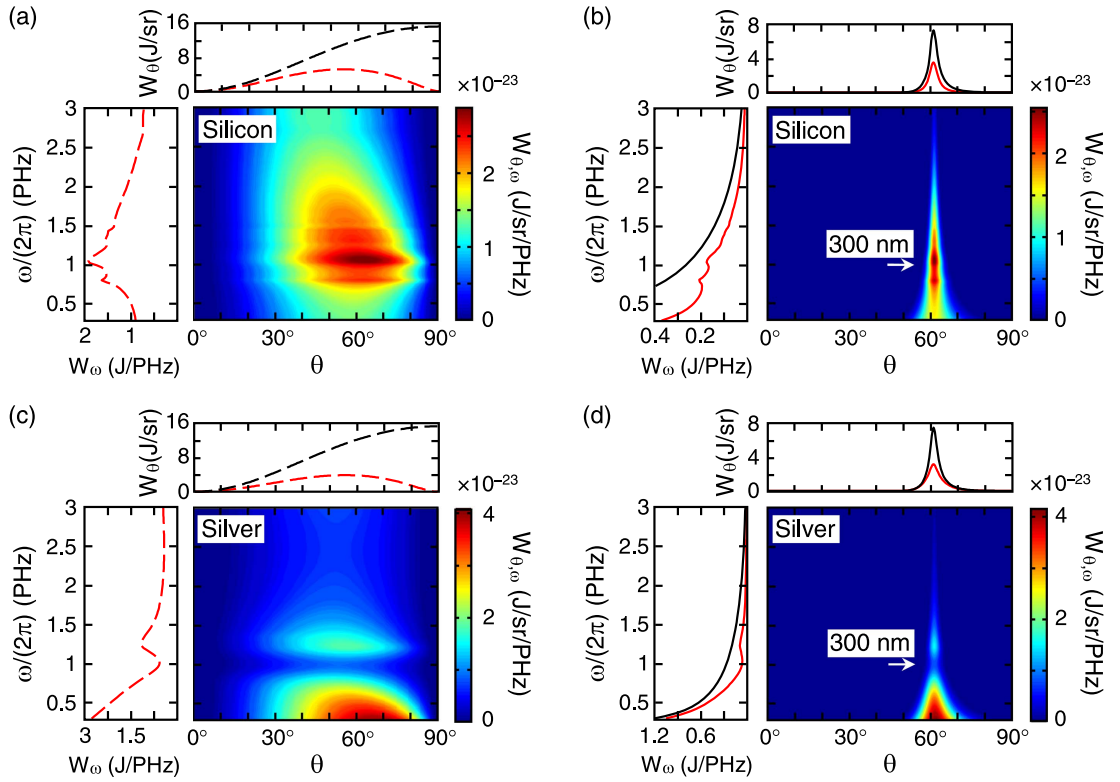

Figure 4. Attosecond electron pulses can be expected to emit visible and ultraviolet CTR when incident on realistic surface materials. (a) Single-particle spectrum $W^1_{\theta,\omega}$ for silicon surface at $\alpha = 0°$. (b) CTR spectrum $W_{\theta,\omega}$ for silicon surface at $\alpha = 17°$, $l_x = 3$ μm, $\tau = 0.1$ fs. (c) The same as in (a), but for silver interface. (d) The same as in (b), but for silver interface. The red curves in the right-side and the top-side plots in (a)–(d) show the integrated quantities W_ω and W_θ, respectively. The black curves in these plots show the perfect-conductor case for comparison. The black line at $\sim 4 \times 10^{-23}$ J/PHz for the frequency-independent perfect-conductor spectrum $W^1_{\theta,\omega}$ is not shown in the right-side plots of (a) and (c) for better readability.

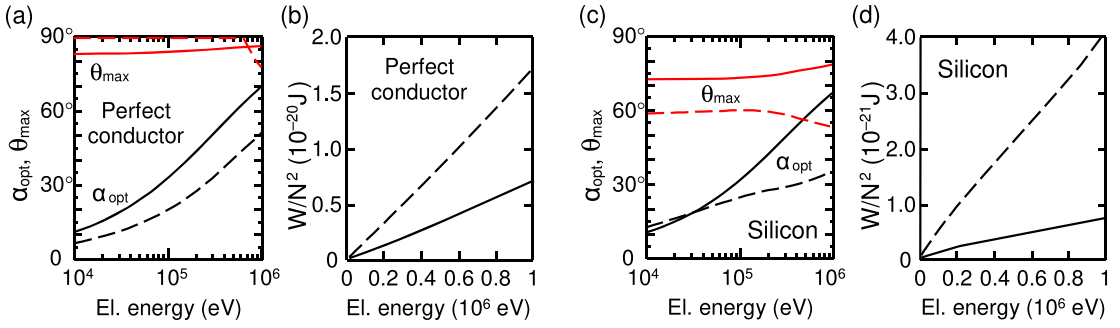

Figure 5. Energy-dependence of the optimal tilt angle and direction of maximum emission for attosecond pulses ($\tau = 0.1$ fs). (a) Optimal tilt angle $\alpha_{\rm opt}$ (black) and the corresponding peak emission (detector) angle $\theta_{\rm max}$ (red) for a perfect-conductor interface. Dashed curves, infinitely small transverse size of the beam; solid curves, $l_x = l_y = 3$ μm. (b) Optimized energy of CTR (normalized by N^2) for a perfect-conductor interface for an infinitely small beam (dashed) and $l_x = l_y = 3$ μm (solid). (c) Same results as in (a) but for a vacuum-silicon interface. (d) Same results as in (b) but for a vacuum-silicon interface.

corresponding optimum angle $\theta_{\rm max}$ for the detector and the resultant overall energy of emission (normalized to N^2) in dependency on the electron energy E in a range from 10 keV to 1 MeV. The pulse duration is $\tau = 0.1$ fs for all cases.

For comparison, we first report the results for an infinitely small beam diameter (dashed curves) and second, for a bunch of realistic finite transverse dimensions ($l_x = l_y = 3$ μm, solid curves). The optimal tilt angle increases with E in all cases, as expected from equation (1), and for sub-relativistic energies is only slightly different from given by equation (1) with $\theta_{\rm max}$ chosen from single-particle emission spectrum as done in above for figure 4. According to further calculations (not shown), the angles $\alpha_{\rm opt}$ and $\theta_{\rm max}$ are independent on τ for perfect conductors and only weakly dependent on τ for Si if τ is short enough to produce a spectrum covering all the high-epsilon range of Si (see figure 4). The angles $\alpha_{\rm opt}$ and $\theta_{\rm max}$ are also only weakly dependent on $l_{x,y}$ as

long as the pulse maintains a 'pancake'-shape. For relativistic electron energies the transition radiation has a double-lobe pattern [59] centered around $\theta \approx \alpha$. This feature results in a discontinuity in figures 5(a) and (c) at the edge of the shown range, $E \approx 1$ MeV, for the infinitely small beam size (dashed curves). For a realistically small but finite beam sizes this discontinuity is not present (solid curves). The range of $E > 1$ MeV is not shown in figure 5 because for such relativistic bunches the energy of transition radiation is weakly dependent on surface tilting excluding grazing incidences. For further discussion of relativistic bunches, see appendix B.

4. Discussion

The above discussed relations now allow us to estimate the practical yield of characteristic CTR that will be emitted in an experiment with few-femtosecond or attosecond electron pulses. We consider four different kinds of attosecond electron pulses or pulse trains that have already been generated or seem realistic in the near future (compare to figure 1). In table 1 we summarize the expected photon yield, wavelengths of emission and other properties of the CTR emission for these four experimental cases. The data in column 1 were calculated for the ponderomotive compression scheme proposed in [30] (compare to figure 1(a)). Electrons move with 1/3 the speed of light and experience periodic acceleration and deceleration via the ponderomotive force in a standing wave of laser light. It was simulated that, based on incoming electron pulses from compact surface emitters [53, 54], about 10 electrons per attosecond pulse can be obtained without too much temporal distortions from space charge [57]. We assume a laser repetition rate of 50 kHz [64, 65]. In order to account for potential experimental difficulties that might not have been considered in [57], we consider here 100-as pulses instead of the predicted 9 as ($1/e$) pulses.

The second example is attosecond pulse trains recently obtained and measured in [34], i.e. a train of 820 as pulses at a repetition rate of 50 kHz. The electron gun of [34] worked in the single-electron regime for which CTR emission is impossible, but based on the availability of better sources [53, 54] and considering the space-charge estimations of [57] we assume here that a number of $N = 3$ electrons per as-pulse should be realistic.

Our third case is isolated few-femtosecond electron pulses from THz compression [24]. In column 3 of table 1 we assume isolated 3 fs electron pulses (no microbunches) [24] with 70 keV central energy and $N = 100$ electrons per pulse in a 50 μm radius beam with 50 kHz repetition rate [24].

Column 4 of table 1 reports the fourth example, relativistic attosecond electron pulses as obtained in [25], where 1 pC, 800 fs bunches of 60 μm radius with 60 MeV central energy are modulated via the inverse free-electron laser process into 410 as microbunches [25]. CTR was already observed from a flat emitter surface at an angle of $\alpha = 45°$and at two selected wavelengths [25]. Here we also report photon flux and spectrum that can be expected from the conical geometry.

For each case listed in table 1, the CTR parameters were calculated for the tilted planar surface (see figure 2(b), 'Tilted' in table 1) and the conical interface (see figure 2(c), 'Cone' in table 1). The CTR energy emitted by a single electron pulse was calculated by equations (2) and (4). In equation (4), we limited the integration to the characteristic wavelength range $\Delta\lambda_{\mathrm{char}}$ defined above, i.e. the spectral emission range in which the pulse duration is most directly encoded. In the last row of table 1, we give the number of photons of CTR per second in the characteristic wavelength range. To calculate this value, we multiplied the photons emitted per attosecond pulse by N_{train} and by the repetition rate of the macrobunches. In reality, there will be optical interference between the emissions of individual pulses of the train. This interference will lead to spectral fringes with a periodicity that corresponds to the separation between the pulses in time. If this separation is much larger than the pulse duration [31, 33, 34], the fringes will not substantially change the spectral envelope of emission or the number of photons as compared to isolated pulses.

The divergences presented in table 1 were calculated using the full angular distributions integrated over $\Delta\lambda_{\mathrm{char}}$. These values are somewhat higher than may be expected from the estimation of λ_{peak} by equation (12) due to the material-dependent and the size-dependent red-shifts of emission that were discussed above. One can take the range of emitted wavelengths from table 1 and use the formulas in the discussion of equation (12) for estimations of divergences.

Table 1 shows that the CTR emitted by attosecond electron pulses of various and different origin can realistically be observed and used for pulse characterization. We note that visible and ultraviolet radiation can be detected with extremely high quantum efficiencies (up to 90%) with photodiodes, photomultipliers or charge-coupled-device cameras. The tens of photons per second expected from the simple tilted-surface geometry may be sufficient for distinguishing different pulse durations via their different spectra with reasonable integration times (few seconds). If such a photon flux is not enough, one can invoke the conical geometry, which provides hundreds-of-times higher CTR yield.

It is worth to note that sub-relativistic few-femtosecond and attosecond pulses can in reality exist only within short distances due to free-space and space-charge dispersion, i.e. ongoing shape changes of the pulses during

Table 1. Expected characteristic CTR photon yield for our tilted emission geometries and for various experimental possibilities for attosecond electron pulse generation.

	1		2		3		4	
Authors, reference for electron beam parameters	Baum and Zewail [30, 57]		Morimoto and Baum [34]		Kealhofer *et al* [24]		Sears *et al* [25]	
Electron beam parameters								
Electron energy	31 keV		70 keV		70 keV		60 MeV	
β	1/3		0.48		0.48		0.999964	
Repetition rate	50 kHz		50 kHz		50 kHz		10 Hz	
Beam size $l_x = l_y$ or $l_\perp$ $(1/e)$	6 μm		50 μm		50 μm		60 μm	
Macrobunch duration (FWHM)	300 fs		1000 fs		5 fs		800 fs	
Electron pulse duration τ $(1/e)$	100 as		480 as		3000 as		246 as	
Total number of electrons in a macrobunch $N_{\text{total}} = N_{\text{train}} \times N$	200		900		10		6.3×10^6	
Number of pulses in a macrobunch N_{train}	20		300		1		300	
Number of electrons per attosecond pulse N	10		3		10		21000	
Transition radiation parameters								
Material	Si		Ag		Ag		Si	
Optimal tilt angle α_{opt}	19°		28°		28°		45°	
Detector angle $\theta_{\max}$	77°		81°		81°		45°	
λ_{peak} for pulse duration τ	133 nm		640 nm		4000 nm		328 nm	
$\Delta\lambda_{\text{char}}$ for pulse duration τ	63–580 nm		300–2800 nm		1900–17400 nm		155–1430 nm	
	Tilted	*Cone*	*Tilted*	*Cone*	*Tilted*	*Cone*	*Tilted*	*Cone*
Emission wavelengths (FWHM, nm)	160–400	130–370	550–3000	450–2100	3000–17000	2500–8000	250–1000	250–1000
Polar divergence $\Delta\theta$ $(1/e^2$ radius)	4.2°	3.7°	3.4°	2.9°	17°	13°	0.25°	0.25°
							double-lobe	
Azimuthal divergence $\Delta\varphi$ $(1/e^2$ radius)	1.1°	360°	0.6°	360°	3°	360°	0.25°	360°
CTR energy per electron in $\Delta\lambda_{\text{char}}$, W/N^2 $(10^{-26}$ J)	3.5	940	2.2	960	9	850	730	73000
Photons s^{-1} in $\Delta\lambda_{\text{char}}$	6	1300	17	6200	19	1400	4×10^7	4×10^9

propagation. These distances are, however, are in all considered cases substantially larger than traveled by a pulse in the course of interaction with the transition radiation emitter. Potential correlations between angles, velocities or positions within the beam will likely also be irrelevant in most cases. Correlations in space can probably not be resolved in the far field; variations of angles and velocity in space and time are typically small enough to be neglected.

Another possibility to achieve velocity-matching for sub-relativistic pulses is to use tilted electron pulses. Tilted optical pulses are common in nonlinear optics and useful, for example, for electron pulse compression [24], THz generation [66], traveling-wave excitation of charge carriers at surfaces [67] or laser-driven electron acceleration [12, 32]. To some extent, the concept reported here is complementary, in applying tilted geometries for light emission by electrons. Sometimes the electron pulses might be tilted themselves, for example if originating from ponderomotive compression in off-axis beams [68], but our concept remains applicable. For an electron bunch with a tilt angle ψ with respect to its propagation direction, equation (9) changes to

$$\Delta k = \left[k_x - \frac{\omega}{v}(\sin\alpha + \tan\psi\cos\alpha)\right] \Big/ \cos\alpha \tag{14}$$

and the velocity matching occurs at $\beta\sin\theta = \sin\alpha + \tan\psi\cos\alpha$. One can use equations (2)–(4) and (11)–(13) with equation (14) instead of equation (9) to calculate the CTR energy for this case. At sub-relativistic electron energies (<100 keV) and for small tilt angles (<30°), the properties of CTR are similar for tilted surfaces and tilted electron pulses. The case of tilted relativistic electron pulses is discussed, for example, in [69].

5. Conclusions

Measuring coherent transition radiation emitted from tilted surfaces allows to characterize the durations of few-femtosecond and attosecond electron pulses at sub-relativistic energies, such as useful for recording atomic-scale light–matter interaction by time-resolved diffraction or microscopy techniques. The concept eliminates the influence of transverse bunch sizes on the emitted spectrum by providing constructive interference for all spectral components, especially the high-frequency ones characteristic of ultrashort pulses. Realistic surface materials (silicon, silver) provide enough visible and ultraviolet photons to characterize few-femtosecond and attosecond electron pulses in a wide variety of experiments. Due to the direct relation between emission wavelength and pulse duration in the tilted geometry via equation (12), our concept should also be useful for characterizing even shorter electron pulses in the few-as or zs regimes, should they eventually be generated.

Appendix A. Calculation of single-particle transition radiation spectrum

Transition radiation of a single particle was extensively studied in the 1950s and 1960s; for a review, see [59, 70]. A comprehensive expression for the backward-emitted transition radiation spectrum $W^{1}_{\Omega,\omega}$ for oblique incidence from vacuum can be found, for example, in [71, 72]. Here, we use more general formulas for electric fields with any polarization [60, 73–76]. We assume an interface between media 1 and 2 with respective dielectric constants $\varepsilon_{1,2}(\omega)$. Formulas (2.6) and (2.7) of [76] give explicit expressions for the energy of p- and s-polarized transition radiation emitted to a unit solid angle in a unit frequency interval for a single particle crossing the flat interface between two semi-infinite media with arbitrary dielectric constants $\varepsilon_{1,2}(\omega)$:

$$W^{1\mathrm{p}}_{\Omega,\omega\ 1,2} = \pm\frac{4\pi^2\omega^3\varepsilon^2_{1,2}\cos\theta_{1,2}}{v_z^2c^2\lambda_{1,2}}(\kappa E_{1,2\kappa} + v_x\cos\varphi E_{1,2x})^2,$$
$$W^{1\mathrm{s}}_{\Omega,\omega\ 1,2} = \pm\frac{4\pi^2\omega\varepsilon_{1,2}\lambda_{1,2}\cos\theta_{1,2}v_x^2\sin^2\varphi}{v_z^2}E^2_{1,2x}. \tag{A.1}$$

Here $v_z = v\cos\alpha$, $v_x = v\sin\alpha$, $\kappa = \sqrt{k_x^2 + k_y^2}$ is the transverse, and $\lambda^2_{1,2} = \varepsilon_{1,2}\omega^2/c^2 - \kappa^2$—the longitudinal wavenumbers [60, 76]. Subscripts 1 and 2 of $W^{1\mathrm{p,s}}_{\Omega,\omega\ 1,2}$ correspond to emission to respective medium (electrons travel from medium 1 to medium 2). The expressions for the components of the radiated electric fields are given in [73] (with a typo corrected in [76]) and run

$$E_{1,2\kappa} = \frac{ei}{2\pi^2}\frac{1}{\lambda_{1,2}\varepsilon_{2,1} - \lambda_{2,1}\varepsilon_{1,2}}\left[\left(\frac{\frac{\varepsilon_{2,1}}{\varepsilon_{1,2}} - \frac{v_z}{\omega}\lambda_{2,1}}{k^2 - \frac{\omega^2}{c^2}\varepsilon_{1,2}} + \frac{-1 + \frac{v_z}{\omega}\lambda_{2,1}}{k^2 - \frac{\omega^2}{c^2}\varepsilon_{2,1}}\right)\lambda_{1,2} + \frac{k_x v_x(k_z - \lambda_{1,2} - \lambda_{2,1})}{\omega}\right.$$
$$\left.\times\left(\frac{1}{k^2 - \frac{\omega^2}{c^2}\varepsilon_{1,2}} - \frac{1}{k^2 - \frac{\omega^2}{c^2}\varepsilon_{2,1}}\right)\right],$$
$$E_{1,2x} = \frac{ei}{2\pi^2}\frac{\lambda_{2,1} - k_z}{\lambda_{1,2} - \lambda_{2,1}}\frac{\omega}{c^2}\left(\frac{1}{k^2 - \frac{\omega^2}{c^2}\varepsilon_{1,2}} - \frac{1}{k^2 - \frac{\omega^2}{c^2}\varepsilon_{2,1}}\right), \tag{A.2}$$

where e is the charge of the single particle and i is the imaginary unit. To calculate the field in medium 1, one should use $k_x = \frac{\omega}{c}\sqrt{\varepsilon_1}\cos\varphi\sin\theta$, $k_y = \frac{\omega}{c}\sqrt{\varepsilon_1}\sin\varphi\sin\theta$, $\lambda_1 = -\frac{\omega}{c}\sqrt{\varepsilon_1}\cos\theta_1$, $\lambda_2 = \frac{\omega}{c}\sqrt{\varepsilon_2 - \varepsilon_1\sin^2\theta_1}$, $k^2 = \kappa^2 + k_z^2$, and $k_x v_x + k_z v_z = \omega$ [60].

Appendix B. Tilted surfaces for relativistic electron pulses

In the case of relativistic ($\beta \approx 1$) particles, the CTR emission is largely determined by the single-particle spectrum $W^1_{\theta,\omega}$, that has a double-lobe pattern maximized at $\theta_{\rm rel} \approx \alpha \pm \gamma^{-1}$, where γ is the gamma-factor [48, 59]. The condition $l_\perp \Delta k \ll l_{||}\,\omega/v$ can be rewritten at the angle $\theta_{\rm rel}$, for $\varphi = 0$, and $\gamma \gg 1$ as

$$l_\perp \cos\alpha \ll l_{||}\,\gamma. \tag{B.1}$$

Thus, for highly relativistic electrons with $\gamma \gg 1$ the requirements on the transverse pulse distribution are largely alleviated at normal incidence and, even more, at grazing incidence. The physical reason behind that is that highly relativistic electrons move at $v \sim c$, thus at any incidence angle they are velocity matched to an electromagnetic wave propagating in the direction of specular reflection $\theta_{vm} \approx \alpha$ (in accord with equation (1) with $\beta \approx 1$). Since $W^1_{\theta,\omega}$ is maximized at $\theta_{\rm rel} \approx \alpha \pm \gamma^{-1} \approx \theta_{vm} \pm \gamma^{-1}$, the beam size influence on emission decreases with increase in γ as $\theta_{\rm rel}$ approaches θ_{vm}. The condition that completely eliminates the transverse size influence, $\Delta k = 0$, can be satisfied mathematically at grazing incidence angles, but does not lead to maximization of the emitted energy because it only maximized the bunch size factor $|\tilde{f}|^2$. Nevertheless, tilting the surface somewhat increases the overall CTR yield also for relativistic bunches. The usefulness of such non-perfect velocity matching can be illustrated by comparison of the CTR spectral density $W^{45^\circ}_\lambda$ for a 45° incidence (commonly used due to its convenience) with the respective value for an optimally tilted surface $W^{\alpha_{\rm opt}}_\lambda$. For example, for $l_\perp = 60$ μm, $\tau = 0.1$ fs pulses incident on a Si surface, $W^{89^\circ}_{300\ {\rm nm}} \sim 2 \cdot W^{45^\circ}_{300\ {\rm nm}}$ at 100 MeV, $W^{88^\circ}_{300\ {\rm nm}} \sim 11 \cdot W^{45^\circ}_{300\ {\rm nm}}$ at 26 MeV, and $W^{67^\circ}_{300\ {\rm nm}} \sim 9 \cdot W^{45^\circ}_{300\ {\rm nm}}$ at 1 MeV. Thus, tilting the surface can be beneficial for electron energies up to several MeV, but becomes less beneficial near 100 MeV and above.

References

[1] Zewail A H 2010 Four-dimensional electron microscopy *Science* **328** 187–93
[2] Santala M K, Reed B W, Raoux S, Topuria T, LaGrange T and Campbell G H 2013 Irreversible reactions studied with nanosecond transmission electron microscopy movies: laser crystallization of phase change materials *Appl. Phys. Lett.* **102** 174105
[3] Lorenz U J and Zewail A H 2014 Observing liquid flow in nanotubes by 4D electron microscopy *Science* **344** 1496–500
[4] Ryabov A and Baum P 2016 Electron microscopy of electromagnetic waveforms *Science* **353** 374–7
[5] Ihee H, Lobastov V A, Gomez U M, Goodson B M, Srinivasan R, Ruan C Y and Zewail A H 2001 Direct imaging of transient molecular structures with ultrafast diffraction *Science* **291** 458–62
[6] Siwick B J, Dwyer J R, Jordan R E and Miller R J D 2003 An atomic-level view of melting using femtosecond electron diffraction *Science* **302** 1382–5
[7] Baum P, Yang D S and Zewail A H 2007 4D visualization of transitional structures in phase transformations by electron diffraction *Science* **318** 788–92
[8] Gulde M, Schweda S, Storeck G, Maiti M, Yu H K, Wodtke A M, Schäfer S and Ropers C 2014 Ultrafast low-energy electron diffraction in transmission resolves polymer/graphene superstructure dynamics *Science* **345** 200–4
[9] Ishikawa T *et al* 2015 Direct observation of collective modes coupled to molecular orbital-driven charge transfer *Science* **350** 1501–5
[10] Frigge T *et al* 2017 Optically excited structural transition in atomic wires on surfaces at the quantum limit *Nature* **544** 207
[11] McNeil B W J and Thompson N R 2010 X-ray free-electron lasers *Nat. Photon.* **4** 814–21
[12] England R J *et al* 2014 Dielectric laser accelerators *Rev. Mod. Phys.* **86** 1337–89
[13] Echternkamp K E, Feist A, Schäfer S and Ropers C 2016 Ramsey-type phase control of free-electron beams *Nat. Phys.* **12** 1000
[14] Baum P 2014 Towards ultimate temporal and spatial resolutions with ultrafast single-electron diffraction *J. Phys. B: At. Mol. Opt. Phys.* **47** 124005
[15] Kasmi L, Kreier D, Bradler M, Riedle E and Baum P 2015 Femtosecond single-electron pulses generated by two-photon photoemission close to the work function *New J. Phys.* **17** 033008
[16] Dwayne Miller R J 2014 Femtosecond crystallography with ultrabright electrons and x-rays: capturing chemistry in action *Science* **343** 1108–16

[17] Mourou G and Williamson S 1982 Picosecond electron-diffraction *Appl. Phys. Lett.* **41** 44–5
[18] Bormann R, Strauch S, Schäfer S and Ropers C 2015 An ultrafast electron microscope gun driven by two-photon photoemission from a nanotip cathode *J. Appl. Phys.* **118** 173105
[19] Hoffrogge J, Stein J P, Krüger M, Förster M, Hammer J, Ehberger D, Baum P and Hommelhoff P 2014 Tip-based source of femtosecond electron pulses at 30 keV *J. Appl. Phys.* **115** 094506
[20] Chatelain R P, Morrison V R, Klarenaar B L M and Siwick B J 2014 Coherent and incoherent electron-phonon coupling in graphite observed with radio-frequency compressed ultrafast electron diffraction *Phys. Rev. Lett.* **113** 235502
[21] Gliserin A, Walbran M, Krausz F and Baum P 2015 Sub-phonon-period compression of electron pulses for atomic diffraction *Nat. Commun.* **6** 8723
[22] Maxson J, Cesar D, Calmasini G, Ody A, Musumeci P and Alesini D 2017 Direct measurement of sub-10 fs relativistic electron beams with ultralow emittance *Phys. Rev. Lett.* **118** 154802
[23] van Oudheusden T, Pasmans P L E M, van der Geer S B, de Loos M J, van der Wiel M J and Luiten O J 2010 Compression of subrelativistic space-charge-dominated electron bunches for single-shot femtosecond electron diffraction *Phys. Rev. Lett.* **105** 264801
[24] Kealhofer C, Schneider W, Ehberger D, Ryabov A, Krausz F and Baum P 2016 All-optical control and metrology of electron pulses *Science* **352** 429–33
[25] Sears C M S *et al* 2008 Production and characterization of attosecond electron bunch trains *Phys. Rev. Spec. Top.—Accel. Beams* **11** 061301
[26] Lundh O *et al* 2011 Few femtosecond, few kiloampere electron bunch produced by a laser-plasma accelerator *Nat. Phys.* **7** 219
[27] Lundh O, Rechatin C, Lim J, Malka V and Faure J 2013 Experimental measurements of electron-bunch trains in a laser-plasma accelerator *Phys. Rev. Lett.* **110** 065005
[28] Bajlekov S I, Heigoldt M, Popp A, Wenz J, Khrennikov K, Karsch S and Hooker S M 2013 Longitudinal electron bunch profile reconstruction by performing phase retrieval on coherent transition radiation spectra *Phys. Rev. ST Accel. Beams* **16** 040701
[29] Heigoldt M, Popp A, Khrennikov K, Wenz J, Chou S W, Karsch S, Bajlekov S I, Hooker S M and Schmidt B 2015 Temporal evolution of longitudinal bunch profile in a laser wakefield accelerator *Phys. Rev. ST Accel. Beams* **18** 121302
[30] Baum P and Zewail A H 2007 Attosecond electron pulses for 4D diffraction and microscopy *Proc. Natl Acad. Sci. USA* **104** 18409–14
[31] Kozák M, Eckstein T, Schönenberger N and Hommelhoff P 2018 Inelastic ponderomotive scattering of electrons at a high-intensity optical travelling wave in vacuum *Nat. Phys.* **14** 121–5
[32] Kozák M, McNeur J, Leedle K J, Deng H, Schönenberger N, Ruehl A, Hartl I, Harris J S, Byer R L and Hommelhoff P 2017 Optical gating and streaking of free electrons with sub-optical cycle precision *Nat. Commun.* **8** 14342
[33] Priebe K E, Rathje C, Yalunin S V, Hohage T, Feist A, Schäfer S and Ropers C 2017 Attosecond electron pulse trains and quantum state reconstruction in ultrafast transmission electron microscopy *Nat. Photon.* **11** 793–7
[34] Morimoto Y and Baum P 2017 Diffraction and microscopy with attosecond electron pulse trains *Nat. Phys.* In production (https://doi.org/10.1038/s41567-017-0007-6)
[35] Baum P, Manz J and Schild A 2010 Quantum model simulations of attosecond electron diffraction *Sci. China Phys., Mech. Astron.* **53** 987–1004
[36] Shao H C and Starace A F 2010 Detecting electron motion in atoms and molecules *Phys. Rev. Lett.* **105** 263201
[37] Shao H C and Starace A F 2016 Imaging population transfer in atoms with ultrafast electron pulses *Phys. Rev.* A **94** 030702
[38] Yakovlev V S, Stockman M I, Krausz F and Baum P 2015 Atomic-scale diffractive imaging of sub-cycle electron dynamics in condensed matter *Sci. Rep.* **5** 14581
[39] Maxwell T J, Behrens C, Ding Y, Fisher A S, Frisch J, Huang Z and Loos H 2013 Coherent-radiation spectroscopy of few-femtosecond electron bunches using a middle-infrared prism spectrometer *Phys. Rev. Lett.* **111** 184801
[40] Geloni G, Ilinski P, Saldin E, Schneidmiller E and Yurkov M 2009 Method for the determination of the three-dimensional structure of ultrashort relativistic electron bunches *Technical Report* DESY 09-069 Deutsches Elektronen-Synchrotron DESY, Hamburg
[41] Geloni G, Ilinski P, Saldin E, Schneidmiller E and Yurkov M 2009 Coherent optical transition radiation as a tool for ultrashort electron bunch diagnostics *Proc. DIPAC09 (Basel, Switzerland)*
[42] Islam M R *et al* 2015 Near-threshold electron injection in the laser-plasma wakefield accelerator leading to femtosecond bunches *New J. Phys.* **17** 093033
[43] Leissner B, Berger C, Siedling R, Tonutti M, Geitz M, Schmidt G and Schmuser P 1999 Bunch length measurements using a martin puplett interferometer at the Tesla Test Facility Linac *Proc. 1999 Particle Accelerator Conf. (New York)*
[44] Lumpkin A H, Dejus R J and Sereno N S 2009 Coherent optical transition radiation and self-amplified spontaneous emission generated by chicane-compressed electron beams *Phys. Rev. Spec. Top.—Accel. Beams* **12** 040704
[45] Mihalcea D, Bohn C L, Happek U and Piot P 2006 Longitudinal electron bunch diagnostics using coherent transition radiation *Proc.: Particle Accelerator Conf., 2005*
[46] Murokh A, Rosenzweig J B, Hogan M, Suk H, Travish G and Happek U 1998 Bunch length measurement of picosecond electron beams from a photoinjector using coherent transition radiation *Nucl. Instrum. Methods Phys. Res.* A **410** 452–60
[47] Saldin E L, Schneidmiller E A and Yurkov M V 2004 A novel diagnostics of ultrashort electron bunches based on detection of coherent radiation from bunched electron beam in an undulator *26th Int. Free Electron Laser Conf. and 11th FEL User Workshop 2004 (Trieste, Italy)*
[48] Settakorn C 2001 Generation and use of coherent transition radiation from short electron bunches *PhD Thesis* Stanford Linear Accelerator Center, Stanford University, Stanford, CA
[49] Zhou T Y, Yang Y L, Sun B G, Tang L L, Lu P, Zhou Z R, Wu F F and Liu X Y 2016 Longitudinal electron bunch diagnostics using coherent transition radiation at the IRFEL *Proc. SPIE* **9684** 968411
[50] Orlandi G L 2002 Coherence effects in the transition radiation spectrum and practical consequences *Opt. Commun.* **211** 109–19
[51] Hirschmugl C J, Sagurton M and Williams G P 1991 Multiparticle coherence calculations for synchrotron-radiation emission *Phys. Rev.* A **44** 1316–20
[52] Baum P 2013 On the physics of ultrashort single-electron pulses for time-resolved microscopy and diffraction *Chem. Phys.* **423** 55–61
[53] Gerbig C, Senftleben A, Morgenstern S, Sarpe C and Baumert T 2015 Spatio-temporal resolution studies on a highly compact ultrafast electron diffractometer *New J. Phys.* **17** 043050
[54] Waldecker L, Bertoni R and Ernstorfer R 2015 Compact femtosecond electron diffractometer with 100 keV electron bunches approaching the single-electron pulse duration limit *J. Appl. Phys.* **117** 044903
[55] Hebeisen C T, Sciaini G, Harb M, Ernstorfer R, Dartigalongue T, Kruglik S G and Miller R J D 2008 Grating enhanced ponderomotive scattering for visualization and full characterization of femtosecond electron pulses *Opt. Express* **16** 3334–41
[56] Kirchner F O, Gliserin A, Krausz F and Baum P 2014 Laser streaking of free electrons at 25 keV *Nat. Photon.* **8** 52–7

[57] Baum P and Zewail A H 2009 4D attosecond imaging with free electrons: diffraction methods and potential applications *Chem. Phys.* **366** 2–8
[58] Feist A, Echternkamp K E, Schauss J, Yalunin S V, Schäfer S and Ropers C 2015 Quantum coherent optical phase modulation in an ultrafast transmission electron microscope *Nature* **521** 200
[59] Ginzbung V L and Tsytovich V N 1990 *Transition Radiation and Transition Scattering* (Boca Raton, FL: CRC Press)
[60] Garibyan G M 1960 Transition radiation for a charged particle at oblique incidence *Sov. Phys.-JETP* **11** 1306–7
[61] Aspnes D E and Studna A A 1983 Dielectric functions and optical parameters of Si, Ge, GaP, GaAs, GaSb, InP, InAs, and InSb from 1.5 to 6.0 eV *Phys. Rev.* B **27** 985–1009
[62] Philipp H R and Ehrenreich H 1963 Optical properties of semiconductors *Phys. Rev.* **129** 1550–60
[63] Wernera W S M, Glantschnig K and Ambrosch-Draxl C 2009 Optical constants and inelastic electron-scattering data for 17 elemental metals *J. Phys. Chem. Ref. Data* **38** 1013
[64] Lahme S, Kealhofer C, Krausz F and Baum P 2014 Femtosecond single-electron diffraction *Struct. Dyn.* **1** 034303
[65] Schneider W, Ryabov A, Lombosi C, Metzger T, Major Z, Fülöp J A and Baum P 2014 800 fs, 330 μJ pulses from a 100 W regenerative Yb: YAG thin-disk amplifier at 300 kHz and THz generation in $LiNbO_3$ *Opt. Lett.* **39** 6604–7
[66] Hebling J, Yeh K-L, Hoffmann M C, Bartal B and Nelson K A 2008 Generation of high-power terahertz pulses by tilted-pulse-front excitation and their application possibilities *J. Opt. Soc. Am.* B **25** B6–19
[67] Baum P and Zewail A H 2006 Breaking resolution limits in ultrafast electron diffraction and microscopy *Proc. Natl Acad. Sci. USA* **103** 16105–10
[68] Hilbert S A, Uiterwaal C, Barwick B, Batelaan H and Zewail A H 2009 Temporal lenses for attosecond and femtosecond electron pulses *Proc. Natl Acad. Sci.* **106** 10558–63
[69] Potylitsyn A P 2016 Spatial coherence in transition radiation from short electron bunches *JETP Lett.* **103** 669–73
[70] Ginzburg V L 1996 Radiation by uniformly moving sources (Vavilov-Cherenkov effect, transition radiation, and other phenomena) *Phys.-Usp.* **39** 973
[71] Silva T F, Bonini A L, Lima R R, Maidana N L, Malafronte A A, Pascholati P R, Vanin V R and Martins M N 2012 Optical transition radiation used in the diagnostic of low energy and low current electron beams in particle accelerators *Rev. Sci. Instrum.* **83** 093301
[72] Ter-Mikaelian M L 1972 *High-Energy Electromagnetic Processes in Condensed Media* (New York: Wiley)
[73] Garibyan G M 1958 To the theory of transition effects in electrodynamics *Izvestia Armenian SSR Acad. Sci.* **11** 7–11
[74] Garibyan G M 1958 Contribution to the theory of transition radiation *Sov. Phys.-JETP* **6** 1079–85
[75] Korhmazyan N A 1958 Transition radiation at oblique incidence of a charge *Izvestia Armenian SSR Acad. Sci.* **11** 87–95
[76] Korhmazyan N A 1962 Polarization of transition radiation in the case of oblique impingement *Izvestia Armenian SSR Acad. Sci.* **15** 115–21